Archaean basalts record evidence of lithospheric extension prior to cratonisation

Marthe Klöcking[a*], Karol Czarnota[b], Ian H. Campbell[c], Hugh Smithies[d], David C. Champion[b,e], D. Rhodri Davies[c]

[a]Institute for Mineralogy, University of Münster, Corrensstr. 24, 48149 Münster, Germany
[b] Geoscience Australia, 101 Jerrabomberra Ave, Symonston, ACT 2609, Australia
[c]The Australian National University, Research School of Earth Sciences, Acton, ACT 0200, Australia
[d]Geological Survey of Western Australia, Mineral House, 100 Plain Street, East Perth, WA 6004, Australia
[e]Granite Resources, PO Box 45, Gungahlin, ACT 2913, Australia

**Email: marthe.kloecking@cantab.net*

Highlights

Archaean basalts record evidence of lithospheric extension prior to cratonisation

Marthe Klöcking, Karol Czarnota, Ian H. Campbell, Hugh Smithies, David C. Champion, D. Rhodri Davies

- Re-evaluation of late Archaean upper mantle dynamics in the Yilgarn craton, based on compilation of >15,000 mafic igneous sample compositions across Australia.
- Primitive, uncontaminated samples are depleted in light rare earth elements, consistent with high degrees of melting at shallow depths.
- Trace element modelling predicts melting at <50 km and potential temperatures ~110–270 °C hotter than present-day ambient mantle.
- Depth and temperature predictions are validated by calculating elevations of extrapolated stratigraphic columns at 2.72 Ga, 2.65 Ga and the present-day.
- Results are consistent with decompression melting under near-ambient Archaean mantle conditions, likely with the contribution of a rising mantle plume.

Archaean basalts record evidence of lithospheric extension prior to cratonisation

Marthe Klöcking[a], Karol Czarnota[b], Ian H. Campbell[c], Hugh Smithies[d], David C. Champion[b,e], D. Rhodri Davies[c]

[a] *Institute for Mineralogy, University of Münster, Corrensstr. 24, 48149 Münster, Germany*
[b] *Geoscience Australia, 101 Jerrabomberra Ave, Symonston, ACT 2609, Australia*
[c] *The Australian National University, Research School of Earth Sciences, Acton, ACT 0200, Australia*
[d] *Geological Survey of Western Australia, Mineral House, 100 Plain Street, East Perth, WA 6004, Australia*
[e] *Granite Resources, PO Box 45, Gungahlin, ACT 2913, Australia*

Abstract

The dynamics of Earth's early mantle remain enigmatic. A wide range of tectonic settings have been proposed for the Archaean eon prior to cratonisation, a time from which few samples are preserved in the geological record. Here, we reexamine this topic by estimating temperatures and depths of melt generation in the late Archaean mantle using a new geochemical data compilation of mafic igneous rocks from the Yilgarn craton, Australia. We combine these results with stratigraphic and geodynamic constraints to better resolve Archaean upper mantle dynamics. The igneous data compilation was screened to identify samples most representative of melting conditions in the convecting mantle and to minimise the effects of crystal fractionation and assimilation of crustal or cumulate material. The dataset predominantly comprises tholeiitic basalts in the well-studied Kalgoorlie terrane that lie at the base of the stratigraphic sequence beneath komatiites, later mafic to felsic volcanic sequences, and the granites that make up the bulk of the Yilgarn cratonic crust. The screened data display depleted MORB-like rare earth element patterns with no evidence of a garnet signature. Forward and inverse modelling of these compositions, assuming a partially depleted peridotite mantle source, predicts melting at depths as shal-

Email address: `marthe.kloecking@cantab.net` (Marthe Klöcking)

low as ∼40 km and mantle potential temperatures elevated by ∼110–270 °C compared to present-day ambient mantle. These results are consistent with decompression melting under near-ambient Archaean mantle conditions. Lithospheric extension and the calculated temperature excess could be caused by non-adiabatic mantle flow ahead of a rising plume and/or melting of the plume head itself.

Keywords: Archaean flood basalt, lithospheric thickness, volcanic geochemistry, trace element modelling, Yilgarn craton

1. Introduction

Plate tectonics shapes the surface of our planet and organises underlying mantle flow. It controls much of Earth's topography, the cycling of volatiles, nutrients, heat flow, and numerous other processes that contribute to Earth's habitability (e.g. Kasting and Catling, 2003; Braun, 2010; Lee et al., 2018). While its importance is clear, the origin of plate tectonics and, in particular, the emergence of the first continents, remain disputed. There are numerous conflicting propositions for Earth dynamics in the Archaean eon and a wide range of ages, anywhere from >4 Ga to <1 Ga, have been suggested for the onset of subduction (e.g. Stern, 2005; Hopkins et al., 2010; Korenaga, 2013; O'Neill and Debaille, 2014; Hastie et al., 2016; Campbell and Davies, 2017; Cawood et al., 2018; Gamaleldien et al., 2024).

The primary reason for this uncertainty is the scarcity of data that document early Earth conditions and processes prior to cratonisation. Primitive mafic volcanic rocks, that are unaffected by secondary crustal processes, are key to discerning upper mantle physical conditions, since the depth and temperature of melting is recorded in the geochemical compositions of magmas (e.g. Gast, 1968; Minster and Allègre, 1978; Albarède, 1983; Hofmann and Feigenson, 1983; Keller and Schoene, 2018). Yet, only a small fraction of the exposed crust preserves Archaean lithologies, of which over two thirds are felsic intrusives that formed in the lead-up and during cratonisation (tonalite-trondhjemite-granodiorite rocks, TTGs, and K-rich granites; Champion and Cassidy, 2007; Hawkesworth et al., 2009). Much of the remainder, greenstone sequences that are dominated by mafic volcanic lithologies but also include ultramafic to felsic metavolcanic and -sedimentary rocks, are also overprinted by later continent-building felsic events (Champion and Cassidy, 2007).

Proposed mechanisms for early Earth dynamics, continent formation and the origin of Archaean mafic volcanic rocks range from stagnant-lid models to lateral tectonics and plume dominated crustal production in a mobile lid setting to modern-style plate tectonic processes such as subduction and rifting. For example, Moore and Webb (2013) simulated a cold and thick lithosphere that developed as a result of frequent volcanic eruptions in a heat-pipe Earth model. Capitanio et al. (2020) demonstrated that continental lithosphere can be produced through protracted slow stretching and depletion via decompression melting. Campbell and Hill (1988) argue for a two-stage process where a long-lived mantle plume first generates the mafic volcanic successions of the greenstone belts; and continued conduction of heat then leads to melting of the base of a pre-existing crust, producing granitic lithologies. Czarnota et al. (2010) propose terrane accretion through cycles of subduction and contraction in a convergent margin followed by mid-orogenic extension. Pawley et al. (2012); Mole et al. (2019) and Smithies et al. (2024) emphasise the importance of intra-continental rifting following terrane accretion.

Each of these dynamic modes has specific implications for geological surface processes and the style of volcanism it can support. For example, a heat-pipe Earth features globally uniform lithospheric thicknesses >100 km that effectively insulate the mantle and maintain high surface heat flow (Moore and Webb, 2013). In this setting, very little lithospheric or surface activity occurs, except for melt extraction from depth through relatively narrow vertical channels (Moore and Webb, 2013; Kankanamge and Moore, 2016). If, in contrast, extensional processes were viable, melting at shallow depths could have occurred, and (pseudo-)tectonic processes similar to those occurring in present-day rift settings could be preserved in the stratigraphic record. If melting is triggered by a mantle plume, temporarily increased mantle potential temperatures would be reflected in larger melt fractions at any given depth of melting (McKenzie and Bickle, 1988). An important distinction between these different cratonisation mechanisms, therefore, are the implied lithospheric thickness and mantle potential temperatures.

The Yilgarn granite-greenstone successions in western Australia comprise one of the largest fragments of Archaean crust preserved on Earth, as well as hosting rich nickel and gold mineralisation (Champion and Cassidy, 2007). Due to this geological and economic significance, the Eastern Goldfields Superterrane, in particular, has been studied in great detail and produced many insights into komatiite petrogenesis and Archaean crust-mantle evolution (e.g. Condie, 1975; Arndt and Lesher, 1992; Campbell and Davies, 2017). In this paper, we present a new geochemical data compilation of mafic igneous compositions from the Yilgarn craton that provide novel insight into volcanic processes prior to the onset of cratonisation. Through careful data screening, only the most primitive and uncontaminated samples are selected that can be used to calculate melt fractions and depth of magma generation. These parameters are then used to derive mantle potential temperature and lithospheric thickness at the time of melting. Based on these results, we conduct a holistic reappraisal of the geodynamic processes in the Eastern Goldfields Superterrane: combining geochemical, geophysical and stratigraphic constraints to better resolve late Archaean upper mantle dynamics and the geodynamic processes leading to cratonisation.

2. Geological Setting and Existing Constraints

The Yilgarn craton is a 3.5–2.6 Ga Archaean terrane in southwestern Australia that is predominantly comprised of metamorphosed volcanic, sedimentary and granitic rocks (Czarnota et al., 2010). Metamorphic grade across the craton varies from greenschist to granulite facies, and many of the original igneous textures and structures are preserved (Swager, 1997). The Yilgarn craton is commonly subdivided into a series of provinces, that are generally younging progressively to the east. The Narryer and South West Terrane in the west of the craton are dominated by granite and granitic gneiss, whereas the Youanmi Terrane and the Eastern Goldfields Superterrane are composed of broadly north-trending greenstone belts separated by extensive granites and granitic gneiss (Figure 1a; Cassidy et al., 2006; Czarnota et al., 2010). Although this structure has been widely interpreted to represent terrane accretion, more recent isotopic mapping has revealed an older NE- to ENE-trending fabric (Mole et al., 2019; Smithies et al., 2024). This old fabric was subsequently disrupted and overprinted by younger NNW-striking rifts associated with the emplacement of the greenstone belts (Pawley et al., 2012; Mole et al., 2019; Smithies et al., 2024).

The Eastern Goldfields Superterrane, with ages ranging between 2810 Ma and 2660 Ma for its supracrustal rocks, is further subdivided into three distinct tectonostratigraphic provinces, one of which, the Kalgoorlie Terrane, is well-known for its komatiite to tholeiitic basalt volcanic association (Cassidy et al., 2006; Czarnota et al., 2010). Abundant granitoid complexes make up at least 65–70% of the surface area of the Eastern Goldfields Superterrane, emplaced at the time of peak regional metamorphism between 2670 and 2650 Ma (Champion and Cassidy, 2007).

The Yilgarn craton has been largely tectonically stable since ∼2.62 Ga, following cratonisation during Neoarchaean orogeny (Cassidy et al., 2006). Numerous different mechanisms for cratonisation have been proposed, that generally invoke melting of a pre-existing lower crust to form granites and the subsequent emplacement of these granites into the upper crust (e.g. Campbell and Hill, 1988; Cassidy et al., 2006; Moyen and Martin, 2012; Korhonen et al., 2025). This crust is stabilised by the removal of elements and phases with low melting point (e.g. Si, K and H_2O) and radioactive elements (K, U and Th), while mafic and ultramafic cumulates are thought to have been removed via delamination or similar processes to provide sufficient buoyancy to the cratonic lithosphere (Campbell and Jarvis, 1984; Flament et al., 2008; Moyen and Martin, 2012; Campbell and Davies, 2017). The composition and thickness of the crust and lithospheric mantle have likely remained largely unchanged since then, although localised modification of the base of the lithosphere through melt infiltration is likely (Occhipinti et al., 2017; Tesauro et al., 2020). As a consequence, present-day lithospheric conditions are likely to closely reflect the Neoarchaean architecture. Today, crustal thickness of the Eastern Goldfields Superterrane measures ∼40 km (Kennett et al., 2018). Based on surface exposure and seismic velocities, about 25% of this crust is estimated to constitute greenstones and 75% to make up the felsic plutonic crust (Drummond, 1988; Champion and Cassidy, 2007; Kositcin et al., 2008). Lithospheric thickness is estimated between 180–220 km (Hoggard et al., 2020).

2.1. Stratigraphy

The known stratigraphy of the Kalgoorlie supergroup, i.e. the sequences associated with the evolution of the Eastern Goldfields Superterrane, is characterised by basal mafic to ultramafic marine volcanics and rare intrusives, overlain by komatiites, a mafic volcanic sequence, felsic volcaniclastic deposits and finally a sedimentary package of sandstones and conglomerates (Figure 1c; Swager, 1997; Sylvester et al., 1997; Kositcin et al., 2008; Czarnota et al., 2010; Said et al., 2010; Barnes et al., 2012). The sequence from basal volcanics to the top of the felsic volcaniclastic unit is locally at least 3–7 km thick (Kositcin et al., 2008). It is likely underlain by continental crustal lithologies of the Youanmi Terrane of unknown thickness, including at least 3 km of pre-2.73 Ga greenstones predominantly composed of submarine basalt and rare thin shale or chert horizons and turbidites (Compston et al., 1986; Nelson, 1997; Kositcin et al., 2008; Czarnota et al., 2010; Smithies et al., 2022). Extensive sedimentation does not occur until after the basaltic volcanism, implying the widespread emergence of the continental crust above sea level in conjunction with cratonisation at that time (Campbell and Hill, 1988; Flament et al., 2008). Periodic thinning of the pre-existing continental crust, as required for submarine depositional settings, has been linked to either crustal spreading caused by high Archaean lower crustal temperatures from increased radiogenic heat production, or to intra-continental rifting (Czarnota et al., 2010; Flament et al., 2011; Smithies et al., 2024).

We here focus on the 2.72–2.69 Ga Kambalda Sequence (also known as Hannans Subgroup) and equivalent units from other localities across large distances within the Eastern Goldfields Superterrane that comprise a marine mafic-ultramafic sequence of basal low-Th basalt (e.g. Lunnon basalt) overlain by uncontaminated komatiites which are in turn overlain by increasingly crustally contaminated basalts (e.g. Devon Consuls and Paringa basalts, see Fig. 1; Lesher and Arndt, 1995; Sylvester et al., 1997; Barnes et al., 2012). Both the basal tholeiitic basalts as well as the later contaminated basalts show clear evidence of deposition in a sub-marine setting, with common pillow structures and rare and minor interlayered hemipelagic sedimentary rocks in the form of sulfidic shales and cherts (Barley et al., 1989; Swager, 1997). However, zircon xenocrysts and other evidence of felsic contamination of the mid- to upper parts of the Kambalda Sequence suggest eruption through pre-existing continental crust (Oversby, 1975; Compston et al., 1986; Campbell and Hill, 1988; Barley et al., 1989; Nelson, 1997; Bateman et al., 2001). In contrast, the progression from submarine greywackes to silicic pyroclastic and associated sedimentary rocks within the Black Flag Group, which overlies the Kambalda Sequence, documents a clear transition to a sub-aerial setting by 2.69 Ga (Barley et al., 1989; Said et al., 2010; Campbell and Davies, 2017).

2.2. Geochemistry

The pre-existing mafic crust below the Kambalda Sequence potentially shows the entire compositional variability of the Youanmi Terrane, including komatiite, banded iron formation and tholeiitic pillow basalt with relatively low MgO concentrations and slight light rare earth element (LREE) depletion, indicating a previously depleted mantle source. Although there is some limited evidence of crustal contamination, these lithologies are predominantly primitive and uncontaminated, in contrast to the overlying Kambalda Sequence (Czarnota et al., 2010; Smithies et al., 2022).

The low-Th basalt at the base of the Kalgoorlie supergroup, represented by the Lunnon basalt in the Kambalda Sequence, is characterised by moderate MgO contents, low incompatible element concentrations with flat REE–HFSE patterns and minor LREE depletion, elevated Cr and Ni, an absence of significant Nb anomalies or other indicators of extensive fractionation or crustal contamination, and ϵNd values between 2.1–3.7 (Lesher and Arndt, 1995; Barnes et al., 2012). Two distinct suites have been distinguished within this basaltic unit, based predominantly on their MgO and incompatible element content. They are interpreted to be variably fractionated melts derived from the same, previously depleted, mantle source by different degrees of partial melting (Redman and Keays, 1985; Lesher and Arndt, 1995). This group represents typical tholeiitic basalts derived by moderate to high degrees of melting at shallow depths (Barnes et al., 2012).

The komatiite sequence comprises ultramagnesian rocks with characteristic spinifex textured flows that are generally interpreted to require high degrees of partial melting ($\geq$30%) at considerable depth (8–12/15 GPa), consistent with melting within a mantle plume (Condie, 1975; Nesbitt and Sun, 1976; Arndt and Lesher, 1992). Arndt and Lesher (1992) proposed a plume with mantle potential temperature, $T_P \simeq 1750$ °C as the source of the Kambalda komatiites. ϵNd values of $\sim$5 are slightly higher than those of the low-Th tholeiitic basalts, which could indicate different melt sources for the two events (Campbell et al., 1989; Lesher and Arndt, 1995).

The top of the sequence is characterised by basaltic rocks with progressive crustal contamination (Lesher and Arndt, 1995; Bateman et al., 2001). Compositions broadly overlap with the underlying komatiitic basalts except for a strong enrichment in LREE and Th, combined with strongly negative Nb anomalies, that suggest combined fractionation and crustal contamination of komatiitic melts (e.g. Barnes et al., 2012). This progressive contamination is also shown in ϵNd values that evolve from 2.5 for the Devon Consuls basalt to -1.6–1.8 for the Paringa basalt at the top of the sequence (Bateman et al., 2001).

3. Data Selection and Screening

It has been demonstrated that primitive volcanic rocks can preserve signatures of melting processes in the mantle (e.g. Gast, 1968; Minster and Allègre, 1978; Albarède, 1983; Hofmann and Feigenson, 1983; McKenzie and O'Nions, 1991; Langmuir et al., 1992; Plank and Forsyth, 2016). The depth and temperature of melting are recorded in magma major and trace element chemistry, along with evidence of any additional processes that occurred during magma storage and ascent. In the most primitive igneous rocks, such additional processes are limited and can often be 'reversed' to estimate primary magma composition (e.g. Lee et al., 2009). We therefore compiled and screened a dataset of the most primitive and uncontaminated samples of Archaean mafic rocks from the Yilgarn craton to calculate their melt fractions and depth of magma generation.

Similarly to Barnes et al. (2012) we did not want to restrict this study to the Kambalda Sequence alone. Through Geoscience Australia's *'Exploring for the Future'* programme, Klöcking et al. (2020) compiled a dataset of more than 10,000 mafic igneous (volcanic and shallow intrusive) sample compositions across Australia from separate major and trace element datasets curated by the Geoscience Australia Inorganic Geochemistry database (GEOCHEM; Champion, 2019) and the state geological surveys. To collate a comprehensive collection of mafic volcanic samples from the Archaean Yilgarn craton in Western Australia, this dataset has been further augmented with additional analyses from the database of the Geological Survey of Western Australia (WACHEM; Geological Survey of Western Australia, 2021). The full dataset comprises >15,000 analyses, of which >3,700 are from greenstones of the Yilgarn craton.

The majority of samples in this igneous data compilation have not been directly dated. Missing ages were assigned by cross-referencing the dataset with the Australian Mafic-Ultramafic Events Dataset (Thorne et al., 2014) and the Australian Stratigraphic Units Database (Geoscience Australia and Australian Stratigraphy Commission, 2017) as well as local stratigraphic relationships. Where dates were available from both of these sources, a 'preferred age' was chosen based on the event or unit description and the uncertainties reported in each dataset. Drill core samples were assigned ages based on the known stratigraphic succession. The data compilation is available at Klöcking et al. (2025).

Only the most primitive melt products can be used to resolve mantle conditions such as the pressure and temperature of melt generation. Secondary processes, including crystal fractionation and assimilation, significantly alter the primary magma composition. As a consequence, geochemical screening of the compiled dataset, based on MgO, Eu, Sr, Pb and Nb/U contents, was required to select those samples that are most similar to the primary melt generated in the mantle. MgO is a proxy for olivine and clinopyroxene fractionation, while Eu is preferentially incorporated into plagioclase compared to the other rare earth elements. Screening by these elements removes any samples that have undergone significant crystallisation or assimilation of minerals such as olivine, clinopyroxene and plagioclase. In this screening process, only the least evolved, basaltic samples that contain 7 wt% $\leq$ MgO $\leq$ 13 wt% were accepted for further analysis. To remove samples affected by plagioclase fractionation or crustal assimilation, only samples with negligible Eu and Sr anomalies of were accepted: $0.9 \leq \frac{Eu}{Eu^*} \leq 1.1$ and $0.75 \leq \frac{Sr}{Sr^*} \leq 1.25$ (where $\frac{Eu}{Eu^*} = \frac{Eu_n}{\sqrt{Sm_n Gd_n}}$; $\frac{Sr}{Sr^*} = \frac{Sr_n}{\sqrt{Nd_n Pr_n}}$; subscript n refers to compositions normalised to primitive mantle of McDonough and Sun, 1995). Furthermore, to screen out samples with the chemical affinity of modern-day subduction-related melts, samples with a positive Pb anomaly ($\frac{Pb}{Pb^*} = \frac{Pb_n}{\sqrt{Nd_n Pr_n}} > 1.1$) were removed. In a final screening step, only samples with Nb/U $>$ 30, an indicator for crustal contamination, were accepted (Figure 2a; Sylvester et al., 1997; Hofmann et al., 1986; Jochum et al., 1986). One additional sample was removed because of its anomalously high Ta concentration. The resultant screened dataset for the Yilgarn craton contains 47 samples (Klöcking et al., 2025).

This screened dataset predominantly comprises tholeiitic basalts in the Kalgoorlie terrane that erupted prior to the main komatiite sequence or the felsic magmas that make up the bulk of the Yilgarn cratonic crust. The mafic compositions investigated here, therefore, represent melting conditions before the onset of processes leading to cratonisation. Although confined predominantly to the Eastern Goldfields Superterrane, they span a large geographical region and mostly belong to several coeval but distinct units (Figure 1). These units include the Lindsays Basalt, Lunnon Basalt, the Desirable Pillow Basalt (Woolyeenyer Formation), Satellite Igneous Complex, the Youanmi Terrane greenstones. In addition, the dataset also includes older samples from the Mount Pleasant Gabbro, Stony Hill Dolerite and Yamarna Terrane greenstones, which are geochemically indistinguishable from the Lunnon Basalt. Following Barnes et al. (2012), we collectively refer to them as basal low-Th basalts.

As shown in Figure 2b, the screened data display depleted, MORB-like rare earth element patterns. The flat mid- to heavy-REE patterns show no evidence of a garnet signature. Anomalies in the fluid mobile, large ion lithophile elements (LILEs: Cs, Rb, Ba) and other small compositional variations could be a consequence of additional contamination, weathering or analytical uncertainties of individual samples not removed by the screening process. Note, however, that the overall sample compositions are remarkably homogeneous, so that their mean concentrations likely reflect source processes. Finally, these screened compositions were corrected for olivine and clinopyroxene fractionation, using the Petrolog3 software of Danyushevsky and Plechov (2011) with the mineral-melt equilibrium models of Langmuir et al. (1992), to obtain near-primary melt compositions that may be used for modelling of the melting process. For each sample, olivine and clinopyroxene were added back into the observed melt composition until it is in equilibrium with forsterite-93 olivine and Mg#-93 clinopyroxene. These equilibrium compositions were chosen based on average Archaean xenolith compositions (Herzberg and Rudnick, 2012). For this calculation, it is assumed that olivine contains no REEs while REE partition coefficients for clinopyroxene are taken from (Oliveira et al., 2020). Due to the low precision of the Petrolog3 output (one decimal place for trace elements), all other trace elements were calculated separately by mass balance from the observed concentrations and the total amount of olivine and clinopyroxene addition. On average, 16% olivine and 31% clinopyroxene were added to the observed melt composition during this fractionation correction. Corrected melt MgO contents range between 17.5–19.6 wt% (average 18.7 wt%).

4. Inverse Geochemical Modelling

Quantitative constraints on the extent and depth range of melting for a volcanic province can be computed by comparing observed REE concentrations with a range of predictions from mantle melting models (McKenzie and O'Nions, 1991). Since REEs are incompatible in the main mantle phases, their concentrations within the melt reduce as melt fraction increases. In addition, heavy REEs are compatible in garnet whereas light REEs are not, which renders REE distributions sensitive to the relative proportions of melting that occur within the garnet and spinel stability fields. Since garnet is only present at depths approximately ≥ 65 km, REE concentrations can, therefore, be used to determine both the depth and temperature of melting (Kay and Gast, 1973; McKenzie and O'Nions, 1991; Jennings and Holland, 2015). For a given mantle composition, the depth of onset of melting is principally controlled by mantle potential temperature, T_p, while we assume that melting ceases at the base of the mechanical lithosphere, z_L (McKenzie and Bickle, 1988). Final melt fraction is determined as the cumulative pool of melts extracted between these two depths, with a weighting towards deeper melts to represent a triangular melting region.

Here, we estimate the melting depth and temperature for the Yilgarn low-Th basalts with a near-fractional decompression melting model. We use the INVMEL-v12 forward model to generate a suite of REE profiles by varying T_p by 1 °C and z_L by 1 km increments between 1250 and 1650 °C and 0 and 100 km, respectively (McKenzie and O'Nions, 1991; White et al., 1992). Based on the εNd composition of the low-Th basalts (εNd $\simeq 3$), we assume a moderately depleted peridotite source composition derived by mixing primitive and depleted end members of McKenzie and O'Nions (1991) in a ratio of 70:30.

The hydrous melting model of Katz et al. (2003) is used to calculate melt fraction as a function of depth for each T_p–z_L pair. Source water content is set relative to the source Ce content (H_2O/Ce = 200; Michael, 1995). Note that, to honour more recently obtained experimental constraints, the values of several parameters used in the Katz et al. (2003) melting model have been revised to those used in Shorttle et al. (2014) and calculations were performed using pyMelt (Matthews et al., 2022). Present-day, ambient mantle potential temperature implied by this parameterisation is ∼1330 °C, which is the temperature required to produce 7 km of oceanic crust at a mid-ocean ridge where asthenospheric mantle is decompressed to surface pressures. Partition coefficients for olivine, orthopyroxene and spinel used by the INVMEL-v12 algorithm are given by McKenzie and O'Nions (1995). Coefficients for clinopyroxene and garnet are calculated using parameterisations described by Wood and Blundy (1997) and Westrenen et al. (2001), respectively. Mineral compositions together with mantle mineralogy as a function of pressure and melt fraction are provided by McKenzie and O'Nions (1991) and McKenzie and O'Nions (1995). We assume that the spinel-garnet transition occurs between 63 and 72 km and does not vary with temperature (i.e. 21–24 kbar; Klöcking et al., 2018). Note that the use of an alternative melting parameterisation or a deeper spinel-garnet transition would increase inferred potential temperature by up to +50°C (Klöcking et al., 2018).

To estimate the melting conditions for the Yilgarn low-Th basalts, the misfit between observed REE concentrations and those calculated from the forward models is minimised. A grid search is carried out to identify models with the smallest root mean squared (rms) misfits between calculated and average observed concentrations, normalised by the sum of their 3σ uncertainties (Figure 3). Only the four elements La, Nd, Dy and Yb are required for the misfit calculation: these commonly measured elements evenly sample the range of REE partition coefficients for spinel and garnet-bearing lithologies and so can be used to derive source processes without bias to either melt fraction or depth of melting. The composition of other elements not included in the misfit calculation provide an independent means to assess the quality of our results. Models are deemed acceptable if they yield rms misfits $\leq$2. This threshold is arbitrary, but reflects a reasonable range of model solutions.

Best-fitting models suggest extensive melting over a $\sim$150 km depth range with maximum melt fractions of $\sim$30% (Fig. 3b). Shallower melting is favoured, although the overall large melt fractions still predict between 10–25% melting within the garnet stability field. Figure 3d shows a clear trade-off between T_p and z_L, where solutions at lower temperatures and shallow depths produce similar melt compositions (due to similar melt fractions) as solutions at higher temperatures and larger depths. Note that uncertainties are large because of the very high melt fractions required by the highly depleted REE compositions: at cumulative melt fractions greater than $\sim$20%, REEs become increasingly insensitive to small variations in T_p and z_L. Only La, Nd, Dy and Yb concentrations are used to determine the minimum misfit in Figure 3d. The good fit to other trace element compositions, therefore, acts as a further control that the model solutions can reasonably predict the full observed elemental compositions (Fig. 3c).

The range of best-fitting solutions predict lithospheric thickness of 0–47 km and mantle potential temperature estimates vary between 1440–1600 °C, i.e. an increase of $\sim$110–270 °C compared to present-day ambient mantle. By extrapolating a secular cooling curve between today and the solidification of Earth at 4.5 Ga at mantle potential temperatures elevated by +190 °C compared to today, we calculate an ambient mantle potential temperature of 1420 °C at 2.7 Ga, or +90 °C above the present-day (*cf.* Davies, 1999; Campbell and Griffiths, 2014). The REE model results therefore predict potential temperatures elevated by $\sim$20–180 °C compared to the late Archaean ambient mantle.

5. Discussion

As previously observed by Barnes et al. (2012), the low-Th basalts display distinctive flat mid- to heavy-REE patterns that show no evidence of a garnet signature. REE modelling suggests that this absence of a garnet signature is due to shallow melting and the overall high melt fractions. Even though melting in the garnet field is predicted, the majority of best-fitting model solutions exceed the threshold of 10% melting for garnet exhaustion at $\leq$3 GPa (Walter, 1998).

The degree of depletion in LREE suggests that an even more depleted peridotite source composition could provide a slightly better fit to observed compositions. However, since the effect on calculated T_p and z_L would be minimal, we have chosen to use the available Nd isotopic compositions to constrain the level of depletion. For comparison, choosing 50% depletion (i.e. a 50:50 mix of primitive and depleted MORB mantle) results in best-fitting predictions of T_p = 1416–1600 °C and z_L = 0–57 km.

Since stratigraphic constraints require pre-existing continental crust, the shallowest melting depths predicted by REE inverse modelling are rejected, and our preferred solutions lie in the range of T_p = 1550–1600 °C and z_L = 40–50 km. Nonetheless, these shallow depths of melting likely require significant amounts of stretching and shortening of the pre-existing continental crust/lithosphere. The thickness of this pre-existing crust and lithospheric mantle are unknown. The only constraints are that all eruptions of the Kambalda Sequence and the previous mafic sequences were submarine and erupted through pre-existing continental lithosphere, which suggests a lack of extensive low-density crust and depleted continental lithospheric mantle.

For mantle melting at T_p = 1550 °C and z_L = 40 km, INVMEL-v12 predicts a total melt thickness of ~20 km at the base of the lithosphere. This melt volume is more than enough to extract the observed thicknesses of the Lunnon Basalt at Kambalda or the Woolyeenyer Basalt at Norseman, both of >1750 m thickness (e.g. Kositcin et al., 2008). Based on the fractionation correction of ~50%, a further 1 km of cumulates could be intruded at the base of the crust; and it is possible that at least part of the remaining melt volume could also have been intruded into the lithosphere and up to the base of the crust. Although there is no evidence preserved in the stratigraphic record of either cumulates or mafic intrusions related to the low-Th tholeiites, it is likely that this voluminous magmatic event would have substantially re-thickened the crust and lithosphere. Later komatiite volcanism likely produced even higher melt volumes. Therefore, despite the originally thin crust predicted here at the time of basal low-Th basalt generation (2.72 Ga), crustal thickness at the time of cratonisation (∼2.65 Ga) could have easily increased to >50 km. The minimum required crustal thickness for cratonisation processes, as defined by the inferred depth of remelting of hydrated mafic crust, is >50 km (Moyen and Martin, 2012), which is plausible to achieve with our results. The present-day crustal thickness of 40 km is then the result of delamination of mafic cumulates during cratonisation and subsequent surface erosion.

The mantle residue produced by melting at $T_p = 1550$ and $z_L = 40$ has a composition of FeO = 7.2 wt% and Mg# = 92. These values are consistent with the compositions of global Archaean xenoliths (Mg# = 92–94; Griffin et al., 1999; Herzberg and Rudnick, 2012; Campbell and Davies, 2017). Finally, the melting conditions predicted by REE modelling also agree with previous estimates of Herzberg et al. (2010) and Lee and Chin (2014) based on major element compositions of different, smaller datasets. They calculated melting depth of 30 km and mantle potential temperatures of 1400–1750 °C. Note that the thermometer of Lee et al. (2009) employed by Lee and Chin (2014) consistently predicts mantle potential temperatures 50–100 °C higher than the McKenzie and O'Nions (1991) model used here (Klöcking et al., 2018). While the melting depths are consistent with the solutions presented here, we are able to constrain a smaller range of possible mantle potential temperatures due to the extensive data screening.

5.1. Geodynamic Setting

A wide range of different geodynamic settings have been proposed for the Eastern Goldfields Superterrane over the years. Many of these proposals invoke mantle plume activity, often in combination with extensional tectonic processes. In contrast, previously popular hypotheses of a convergent margin type setting with calc-alkaline volcanism (e.g. Barley et al., 1989; Swager, 1997; Krapez et al., 2000; Kositcin et al., 2008) now seem less likely based on more recent evidence (Mole et al., 2019; Smithies et al., 2024).

Komatiite volcanism, in particular, is commonly attributed to melting within a mantle plume (Condie, 1975; Nesbitt and Sun, 1976; Arndt and Lesher, 1992; Lesher and Arndt, 1995). Campbell et al. (1989) further suggested that the low-Th basalts could have been produced by the head of a plume, whereas melting of the plume tail generated the hotter and deeper komatiitic melts. Heat derived from such a plume and large-volume magmatic intrusions could then cause melting of the pre-existing continental crust leading to crustal contamination of later volcanic sequences and extensive granite formation (e.g. Campbell and Hill, 1988; Campbell and Davies, 2017; Moyen and Laurent, 2018). The distinctive north-south orientation of the Eastern Goldfields mafic and ultramafic successions, as well as the larger E–W spatial extent of plume-head-derived basalts compared to the more restricted plume-tail-derived komatiites, could also be explained by lateral diversion of a plume impinging under the thick continental lithospheric lid of the Youanmi Terrane, in turn triggering continental rifting along the craton margin (Barnes et al., 2012).

Extension is a critical feature of all proposed geodynamic scenarios as it is unequivocally documented by the stratigraphic record, and regardless of the geodynamic trigger, the volcano-sedimentary successions of the greenstone belts across the Eastern Goldfields Superterrane are often interpreted as contemporaneous basins (Swager, 1997; Czarnota et al., 2010; Barnes et al., 2012). Various trigger mechanisms of this extension have been suggested, ranging from modern-style intracratonic rifting, to more short-lived, episodic lithospheric extension and gravity-induced lateral flow (Flament et al., 2011; Capitanio et al., 2020). It has been suggested that both stratigraphic and geochemical characteristics of the Eastern Goldfields Superterrane can be explained through repeated continental rifting in combination with plume-derived magmatism (Pawley et al., 2012; Mole et al., 2019; Smithies et al., 2024). Our results are consistent with this interpretation, where both shallow melting depth and elevated mantle potential temperatures are required. As pointed out by many previous authors, the low-Th basalts are most consistent with shallow melting and, therefore, an extensional setting. Stratigraphic relations necessitate that this extension occurs on pre-existing continental crust (Czarnota et al., 2010). We therefore disregard the best-fitting model result that suggests melting without any overlying crust or lithosphere ($z_L = 0$). However, misfit significantly increases for z_L >50 km which is therefore considered an upper bound on lithospheric thickness during melting. The calculated mantle potential temperature is elevated compared to present-day values, however it is significantly lower than the plume $\mathrm{T}_P \simeq 1750$ °C proposed by Arndt and Lesher (1992) and others for the generation of the later komatiites. Instead, the calculated T_p range includes solutions only ∼100–250 °C hotter than present-day ambient mantle, which is only slightly elevated above temperature projections for the Archaean mantle and estimates of the secular cooling of the Earth (i.e. ≤+90 °C; Jarvis and Campbell, 1983; Richter, 1988; Nisbet et al., 1993).

The results from REE modelling are consistent with decompression melting of a slightly hotter Archaean mantle, induced by moderate extension of the pre-existing lithospheric lid, but also with the more elevated temperatures of a mantle plume head. Since the filtered dataset comprises samples with significant spatial and temporal variability, similar melting conditions must have been present at multiple times and possibly also at multiple locations. Although this periodicity would be easier to explain with purely extensional-driven melting, the required temperature excess for deeper melt derivation does point towards the contribution of a mantle plume. It is, of course, also possible that the different magmatic events are the result of similar melting extents produced by distinct combinations of T_p and z_L.

Since the present study only examines the low-Th basalts erupted prior to the main komatiite sequences across the Eastern Goldfields Superterrane, it cannot fully reconcile or (dis)prove either of the previous geodynamic proposals. Nonetheless, our results require melting of a somewhat depleted peridotite source at shallow depths and moderately elevated temperatures. The extension required to trigger melting could be derived either from stresses above a rising plume head or from lateral tectonic processes that Capitanio et al.

(2020) suggest were more prevalent in the weaker Archaean lithosphere. Our results support a plume origin for the later komatiite sequences, and ultimately TTG formation and cratonisation in response to this heat input, as suggested by Campbell et al. (e.g. 1989); Arndt and Lesher (e.g. 1992); Nisbet et al. (e.g. 1993). In contrast to the previous plume models, however, we argue that the low-Th basalts at the base of the succession predate the arrival of the main part of the plume and represent near-ambient mantle conditions of the late Archaean times in an extensional setting (Fig. 4). The excess heat suggested by our model results could indicate a contribution from the head of the rising plume, although a significant proportion of decompression melting of the ambient upper mantle is also possible. This conclusion is supported by previous suggestions of genetic differences between low-Th basalts and overlying komatiites: Lunnon basalt and Kambalda komatiite have ε_{Nd} values of 2–3.7 and >4, respectively, indicating that they could be derived from different mantle sources (Campbell et al., 1989; Lesher and Arndt, 1995).

5.2. Isostatic considerations

As a final test of our preferred geodynamic setting for the early Eastern Goldfields Superterrane, we have performed isostatic calculations to verify if the proposed lithospheric thickness and mantle potential temperatures are consistent with the changing depositional environments recorded in the stratigraphic record. The Kambalda Sequence records a clear evolution from submarine to subaerial setting, where the low-Th basalts are still erupted below sea level but significant uplift must have occurred by the end of the komatiite and later basaltic events. Figure 4 summarises a possible sequence of events and the respective lithospheric structure used for isostatic calculations.

We balance extrapolated stratigraphic columns from the Kalgoorlie region at 2.72 Ga, 2.69 Ga and its present-day cratonic architecture against a present-day mid-oceanic ridge. Following the approach of Klöcking et al. (2018), the elevation of a continental column is calculated relative to the density structure of a mid-oceanic ridge, based on the thicknesses and densities of crustal, lithospheric and asthenospheric mantle components. We use present-day continental lithospheric thickness of 220 km as the compensation depth. Lithospheric and asthenospheric mantle densities are functions of pressure and temperature. We assume an asthenospheric temperature gradient of 0.44 °C km^{-1}, a pressure gradient of 0.033 GPa km^{-1}, a reference mantle density of 3.33 Mg m^{-3}, a thermal expansion coefficient of 3.3×10^{-5} °C^{-1}, and a bulk modulus of 115.2 GPa. Crustal and lithospheric thickness, crustal density, continental lithosphere depletion and mantle potential temperature are variable, with values used for each calculation given in Table 1. Note that in all of these calculations lithospheric thickness is inclusive of crustal thickness, i.e. the lithosphere comprises both mantle and crustal lithologies.

With the present-day crustal thickness of 40 km, lithospheric thickness of 220 km, ambient mantle T_p and a crustal density of 2.74 Mg m^{-3} based on a 25:75 ratio of mafic and felsic lithologies, this isostatic calculation is able to match present-day elevations of 400 m above sea level (Fig. 4i).

At ∼2.72 Ga, just before the onset of the Kambalda Sequence magmatism, the lithosphere was likely composed of Youanmi-Terrane continental crust and mantle, of which ∼3 km of mafic crust are exposed in the stratigraphic record (Kositcin et al., 2008). Although the crustal thickness at this time is unknown, it must be at least 5–10 km and

Time (Ga)	z_L (km)	z_c (km)	ρ_c (Mg m^{-3})	$\Delta\rho_L$ (Mg m^{-3})	T_p (°C)	u (km)
>2.72	50	15	2.8	0	1420	-0.77
2.72 (pre)	40	10	2.8	0	1550	-0.42
2.72 (post)	110	30	2.9	0	1550	-0.06
2.65	180	50	2.9	0.015	1420	0.64
0	220	40	2.74	0.015	1330	0.39

Table 1: Calculated elevations, u, and variable parameters used for isostatic calculations of the Kalgoorlie region at different times. The two rows at 2.72 Ga refer to conditions immediately pre- and post-eruption of low-Th basalts. z_L = lithospheric thickness; z_c = crustal thickness; ρ_c = crustal density; $\Delta\rho_L$ = continental lithosphere depletion, values from Crosby et al. (2010); T_p = mantle potential temperature.

a submarine setting is required both for the eruption of the pre-existing mafic crust and the low-Th basalts. For this pre-Kambalda column, crustal thicknesses of $\leq$15–20 km in combination with lithospheric thickness of $\sim$40–60 km at ambient mantle potential temperature satisfy elevations below sea level, assuming a crustal density of 2.8 Mg m^{-3} that resembles roughly equal proportions of Youanmi continental crust and denser mafic melts. For example, assuming lithospheric and crustal thicknesses of 50 and 15 km, respectively, predicted elevations are –770 m (Fig. 4g).

At $\sim$2.72 Ga, the low-Th basalts at the base of the Kambalda Sequence are then generated by moderate amounts of extension of this pre-existing lithosphere and the arrival of a heat anomaly, for example from the rising head of a mantle plume. REE model results predict lithospheric thickness of $\sim$40 km and T_p of $\sim$1550 °C, implying a stretching factor of $\sim$0.8. Assuming constant stretching factors for both crust and mantle, we deduce a crustal thickness of $\sim$10 km, and elevations immediately before the emplacement of the low-Th basalts are predicted to be –420 m (Table 1). More elevated mantle potential temperatures would increase elevations above sea level. For example, if we instead assume T_p of 1700 °C at 2.72 Ga, lithospheric thickness would need to be $\geq$80 km to still guarantee a submarine setting. Such high lithospheric thickness is inconsistent with our REE modelling and would not be able to produce melts with the depleted chemical signature of the low-Th basalts.

The total melt volume predicted by INVMEL-v12 at these conditions would have increased crustal thickness by up to 20 km (see discussion above), as well as further increasing overall crustal density. In turn, the highly depleted mantle residue left after 30% melt extraction, would also increase total lithospheric thickness. To satisfy submarine eruptive settings even after low-Th basalt emplacement, assuming a crustal thickness of 30 km and the persistence of the thermal anomaly, lithospheric thickness is required to increase to 110 km. Subsequent komatiite emplacement and later mafic magmatism would further increase crustal thickness to 50 km or more, as required for TTG production. By 2.62 Ga, therefore, addition of $\gg$20 km of predominantly mafic crust could have raised elevations to above +640 m, even after the dissipation of the mantle thermal anomaly (Fig. 4h). Crustal reworking during TTG production, delamination of mafic roots and conductive cooling and thickening of the lithospheric root would then gradually have reduced elevations to present-day values (Fig. 4i).

6. Conclusions

We use a new compilation of mafic volcanic compositions from the eastern Yilgarn craton to reassess late Archaean geodynamic processes in the Eastern Goldfields Superterrane prior to cratonisation. Widespread, relatively homogeneous depleted tholeiitic basalts across the entire terrane suggest melt generation at shallow depths and high melt fractions. REE modelling predicts lithospheric thickness <50 km and mantle potential temperatures elevated by ∼110–270 °C compared to present-day ambient mantle. Isostatic calculations based on these results and stratigraphic constraints predict surface elevations that match the observed evolution from submarine to subaerial deposition during basalt and komatiite emplacement. These results suggest that basal low-Th basalts are the result of decompression melting at Archaean near-ambient mantle temperatures below pre-existing crust and thin lithospheric mantle in an extensional setting. Moderately elevated mantle potential temperatures suggest the contribution of heat from a rising plume head. Extension could either be caused by far-field stresses above the rising plume head or lateral stresses.

Data and Software Availability

The mafic igneous data compilation for Australia is published as Klöcking et al. (2025) in the DIGIS geochemical data repository hosted by GFZ Data Services. The screened dataset, as well as software for data screening, misfit calculations and isostatic balances is available on Zenodo/GitHub (Klöcking, 2025). INVMEL-v12 software was developed and is owned by D. McKenzie to whom requests for access should be directed.

CRediT authorship contribution statement

MK: Conceptualization, Methodology, Formal analysis, Data curation, Writing - Original draft preparation, Writing - Reviewing and Editing. KC: Conceptualization, Methodology. IHC: Writing - Reviewing and Editing. HS: Data curation, Writing - Reviewing and Editing. DCC: Data curation. DRD: Conceptualization, Writing - Reviewing and Editing.

Acknowledgements

This work was made possible by the the Australian government's "Exploring for the Future" programme undertaken by Geoscience Australia. We are grateful to J. Lowrey for help with the data compilation. D. McKenzie generously provided access to INVMEL-v12 software package. Figures were prepared using Generic Mapping Tools, Matplotlib and Inkscape software. MK is supported by the German Research Foundation (DFG grant number KL3162/3-1; 503863705).

Figures

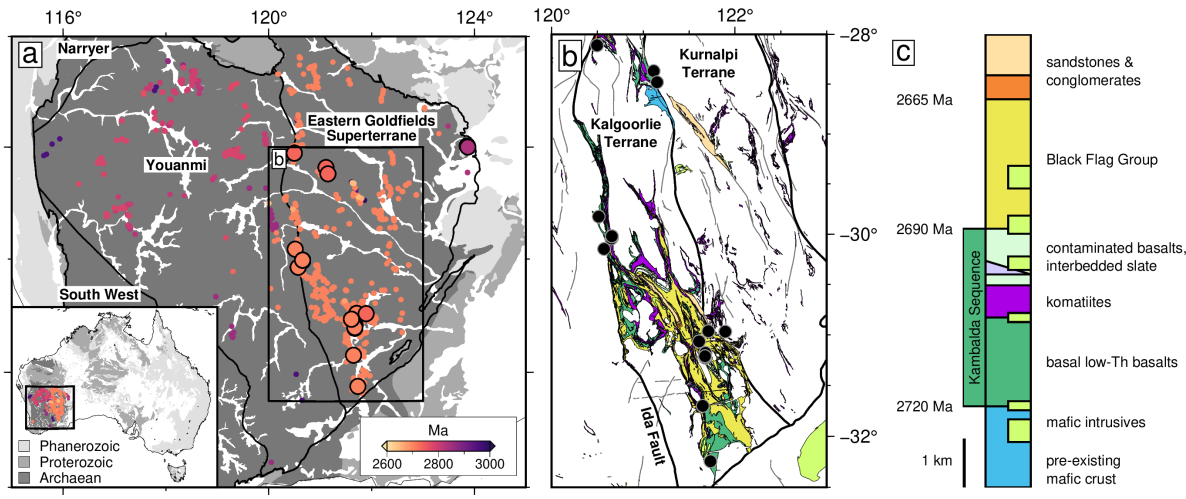

Figure 1: Mafic and ultramafic igneous stratigraphy in the Yilgarn craton. a) Distribution of all igneous samples coloured by age. Larger symbols indicate samples that pass screening for primitive, uncontaminated compositions (see Section 3 for further information). Background coloured by crustal age; black lines = craton/terrane boundaries. b) Mafic and ultramafic igneous units from 1:500 000 State interpreted bedrock geology of Western Australia (2020), coloured according to stratigraphic units in c); thin grey lines = fault lines; thick black lines = province boundaries from Cassidy et al. (2006); black circles = distribution of screened samples. c) Representative stratigraphic column based on GSWA 2018 Eastern Goldfields stratigraphy; approximate unit thicknesses after Kositcin et al. (2008).

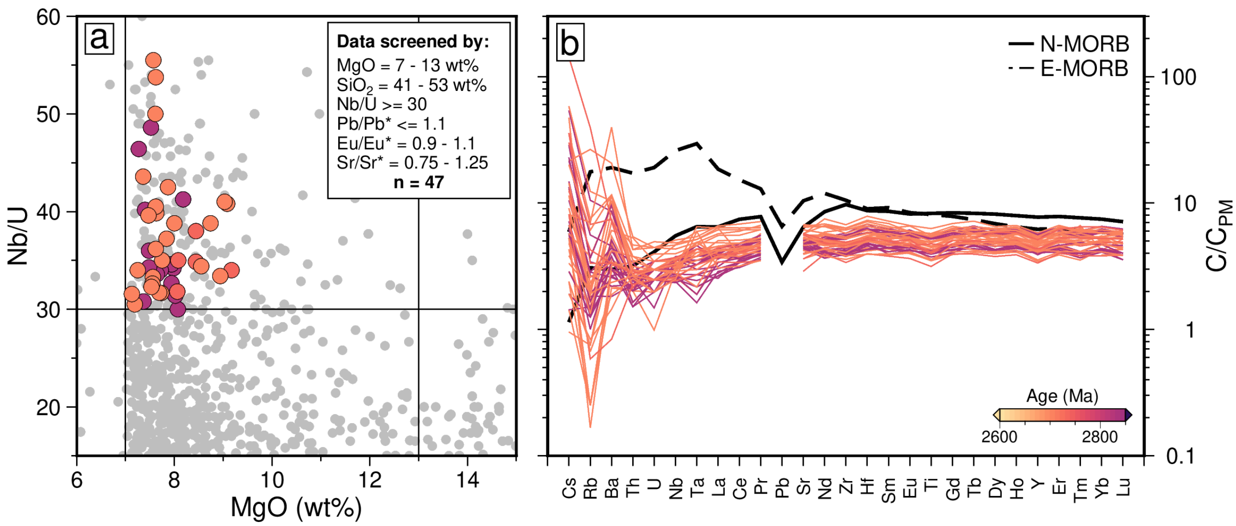

Figure 2: Geochemical characteristics of screened dataset. a) MgO against Nb/U to illustrate data screening process. Large circles = screened samples coloured by age; small grey circles = (ultra-)mafic samples that did not pass screening. Screening criteria are summarised in inset. b) Trace element distribution of screened dataset, coloured by sample age and normalised to primitive mantle composition (PM; McDonough and Sun, 1995). Composition of representative present-day normal and enriched mid-ocean ridge basalt shown to highlight extreme depletion of Yilgarn samples (N- and E-MORB, respectively; Gale et al., 2013).

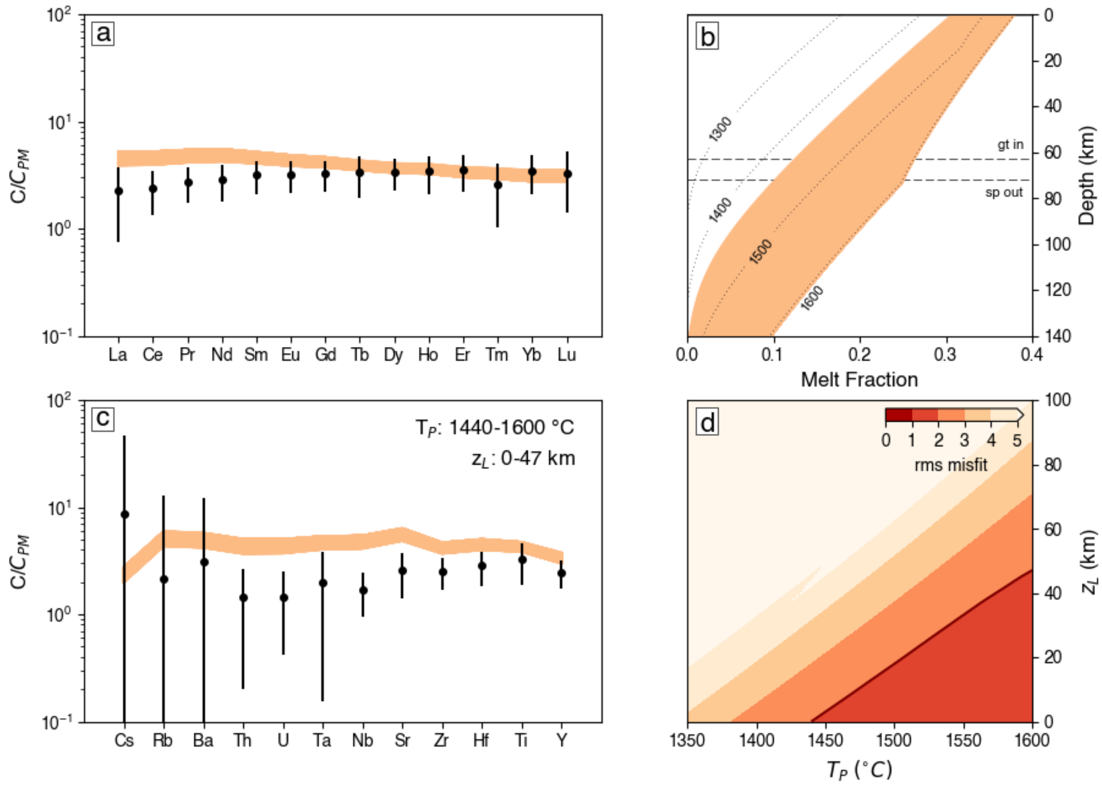

Figure 3: Results from inverse modelling of mean composition of screened dataset corrected for olivine fractional crystallisation. (a) Observed and calculated REE concentrations normalised to primitive mantle. Circles with vertical bars = mean observed concentrations $\pm$ 3σ; black line = best-fit concentrations calculated by inverse modelling; orange polygon = models with rms misfit $\leq$2. Note that only La, Nd, Dy and Yb were used to calculate misfit. (b) Calculated melt fraction as function of depth. Solid black line = melt fraction obtained by fitting average REE composition shown in (a), where the change in slope is due to exhaustion of clinopyroxene from the mantle source; dotted lines = isentropic melting curves labelled according to potential temperature; dashed lines = phase boundaries for spinel and garnet. c) Same as a) for trace element concentrations. These elements were not used in misfit calculation. Predicted potential temperature (T_P) and lithospheric thickness (z_L) shown in top right. d) Range of T_P and z_L tested, coloured by rms misfit. Envelope of darkest red region = rms misfit $\leq$2. Note that during fractionation correction Tm and all trace elements in c) are corrected by mass balance only, which likely leads to an underestimate of their concentrations in the final melt.

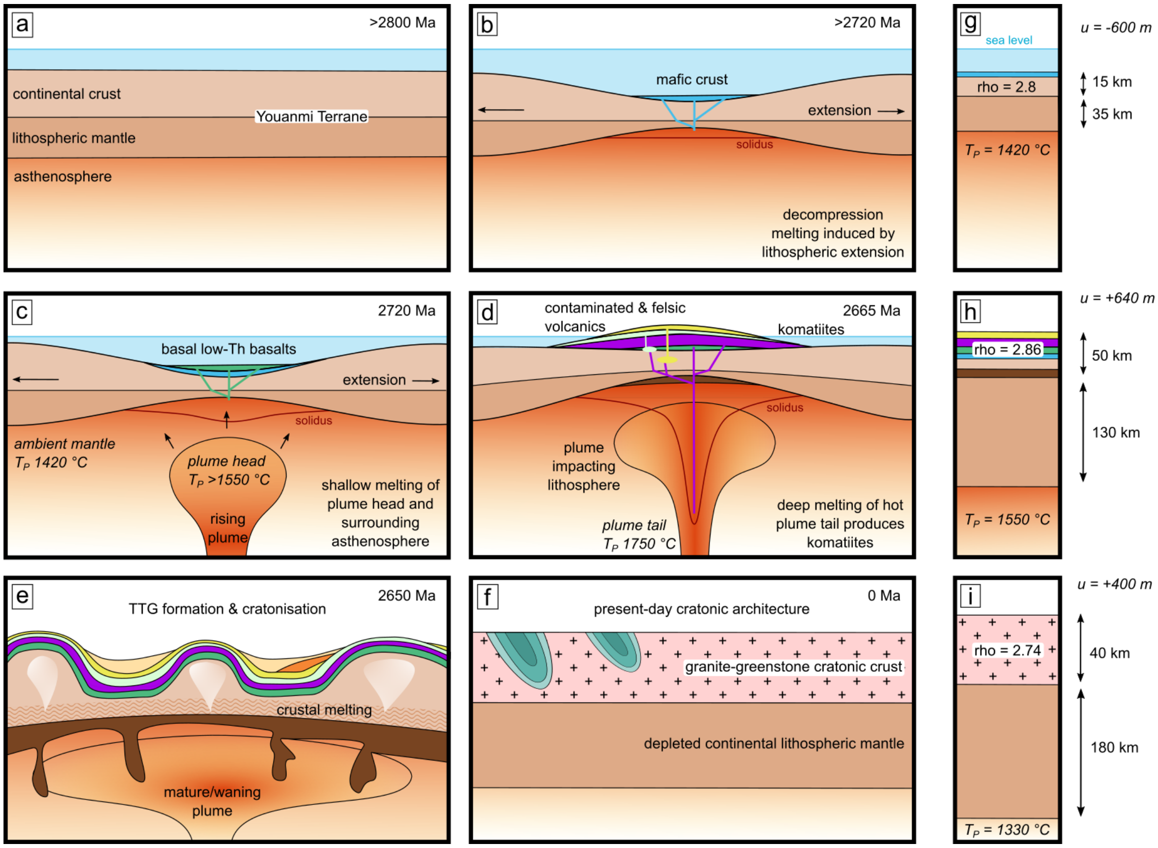

Figure 4: Cartoon summarising the possible geodynamic setting leading to the eruption of basal low-Th basalt and komatiites in the eastern Yilgarn craton (not to scale; ages representative of the Kambalda region). The scenario combines several episodes of lithospheric extension with the plume head-and-tail hypothesis suggested by Campbell et al. (1989), followed by cratonisation after Campbell and Davies (2017). (a–b) Extension of pre-existing Youanmi continental crust/lithosphere leads to eruption of submarine mafic basalts (blue) to form the pre-existing mafic crust. (c) The arrival of an upwelling mantle plume induces further extension, where melts from the plume head mix with decompression melting of the ambient mantle to form the basal low-Th basalts (green). (d) Deep melts derived from the hot plume tail result in komatiite volcanism (purple); mixing of komatiitic melts with tholeiitic intrusions, crustal assimilation and fractionation generate contaminated basalts (mint) and felsic volcanics of the Black Flag Group (yellow). Mafic to ultramafic intrusives form in the lower crust (brown). (e) Large-scale crustal reworking and delamination of dense, ultramafic lithologies during cratonisation. (f) Present-day stable continental architecture of predominantly granitic (pink) crust with greenstone belts (green), above depleted lithospheric mantle. (g–i) Isostatic columns that are balanced against a modern-day mid-oceanic ridge; representative of unit thicknesses in panels b), d) and f), respectively.

References

Albarède, F., 1983. Inversion of batch melting equations and the trace element pattern of the mantle. Journal of Geophysical Research: Solid Earth 88, 10573–10583. doi:10.1029/JB088iB12p10573.

Arndt, N.T., Lesher, C.M., 1992. Fractionation of REEs by olivine and the origin of Kambalda komatiites, Western Australia. Geochimica et Cosmochimica Acta 56, 4191–4204. doi:10.1016/0016-7037(92)90260-P.

Barley, M.E., Eisenlohr, B.N., Groves, D.I., Perring, C.S., Vearncombe, J.R., 1989. Late Archean convergent margin tectonics and gold mineralization: A new look at the Norseman-Wiluna Belt, Western Australia. Geology 17, 826. doi:10.1130/0091-7613(1989)017¡0826:LACMTA¿2.3.CO;2.

Barnes, S.J., van Kranendonk, M.J., Sonntag, I., 2012. Geochemistry and tectonic setting of basalts from the Eastern Goldfields Superterrane. Australian Journal of Earth Sciences 59, 707–735. doi:10.1080/08120099.2012.687398.

Bateman, R., Costa, S., Swe, T., Lambert, D., 2001. Archaean mafic magmatism in the Kalgoorlie area of the Yilgarn Craton, Western Australia: A geochemical and Nd isotopic study of the petrogenetic and tectonic evolution of a greenstone belt. Precambrian Research 108, 75–112. doi:10.1016/S0301-9268(00)00148-0.

Braun, J., 2010. The many surface expressions of mantle dynamics. Nature Geoscience 3, 825–833. doi:10.1038/ngeo1020.

Campbell, I.H., Davies, D.R., 2017. Raising the continental crust. Earth and Planetary Science Letters 460, 112–122. doi:10.1016/j.epsl.2016.12.011.

Campbell, I.H., Griffiths, R.W., 2014. Did the formation of DPrime; cause the Archaean-Proterozoic transition? Earth and Planetary Science Letters 388, 1–8. doi:10.1016/j.epsl.2013.11.048.

Campbell, I.H., Griffiths, R.W., Hill, R.I., 1989. Melting in an Archaean mantle plume: Heads it's basalts, tails it's komatiites. Nature 339, 697–699. doi:10.1038/339697a0.

Campbell, I.H., Hill, R.I., 1988. A two-stage model for the formation of the granite-greenstone terrains of the Kalgoorlie-Norseman area, Western Australia. Earth and Planetary Science Letters 90, 11–25. doi:10.1016/0012-821X(88)90107-0.

Campbell, I.H., Jarvis, G.T., 1984. Mantle convection and early crustal evolution. Precambrian Research 26, 15–56. doi:10.1016/0301-9268(84)90016-0.

Capitanio, F.A., Nebel, O., Cawood, P.A., 2020. Thermochemical lithosphere differentiation and the origin of cratonic mantle. Nature 588, 89–94. doi:10.1038/s41586-020-2976-3.

Cassidy, K.F., Champion, D.C., Krapež, B., Barley, M.E., Brown, S.J.A., Blewett, R.S., Groenewald, P.B., Tyler, I.M., 2006. A revised geological framework for the Yilgarn Craton, Western Australia. Technical Report. Geological Survey of Western Australia. URL: `www.doir.wa.gov.au/gswa/onlinepublications`.

Cawood, P.A., Hawkesworth, C.J., Pisarevsky, S.A., Dhuime, B., Capitanio, F.A., Nebel, O., 2018. Geological archive of the onset of plate tectonics. Philosophical Transactions of the Royal Society A: Mathematical, Physical and Engineering Sciences 376. doi:10.1098/RSTA.2017.0405.

Champion, D., 2019. Inorganic Geochemistry Database. doi:10.26186/129306.

Champion, D.C., Cassidy, K.F., 2007. An overview of the Yilgarn Craton and its crustal evolution, in: Bierlein, F.P., Knox-Robinson, C.M. (Eds.), Proceedings of Geoconference (WA) Inc Kalgoorlie '07. Old Ground New Knowledge, Geoscience Australia. pp. 8–13.

Compston, W., Williams, I.S., Campbell, I.H., Gresham, J.J., 1986. Zircon xenocrysts from the Kambalda volcanics: age constraints and direct evidence for older continental crust below the Kambalda-Norseman greenstones. Earth and Planetary Science Letters 76, 299–311. doi:10.1016/0012-821X(86)90081-6.

Condie, K.C., 1975. Mantle-plume model for the origin of Archaean greenstone belts based on trace element distributions. Nature 258, 413–414. doi:10.1038/258413a0.

Crosby, A.G., Fishwick, S., White, N., 2010. Structure and evolution of the intracratonic Congo Basin. Geochemistry, Geophysics, Geosystems 11, 1–20. doi:10.1029/2009GC003014.

Czarnota, K., Champion, D., Goscombe, B., Blewett, R., Cassidy, K., Henson, P., Groenewald, P., 2010. Geodynamics of the eastern Yilgarn Craton. Precambrian Research 183, 175–202. doi:10.1016/J.PRECAMRES.2010.08.004.

Danyushevsky, L.V., Plechov, P., 2011. Petrolog3: Integrated software for modeling crystallization processes. Geochemistry, Geophysics, Geosystems 12, 1–32. doi:10.1029/2011GC003516.

Davies, G.F., 1999. Dynamic Earth: Plates, Plumes and Mantle Convection. Cambridge University Press, Cambridge. doi:10.1017/CBO9780511605802.

Drummond, B.J., 1988. A review of crust/upper mantle structure in the Precambrian areas of Australia and implications for Precambrian crustal evolution. Precambrian Research 40-41, 101–116. doi:10.1016/0301-9268(88)90063-0.

Flament, N., Coltice, N., Rey, P.F., 2008. A case for late-Archaean continental emergence from thermal evolution models and hypsometry. Earth and Planetary Science Letters 275, 326–336. doi:10.1016/J.EPSL.2008.08.029.

Flament, N., Rey, P.F., Coltice, N., Dromart, G., Olivier, N., 2011. Lower crustal flow kept Archean continental flood basalts at sea level. Geology 39, 1159–1162. doi:10.1130/G32231.1.

Gale, A., Dalton, C.A., Langmuir, C.H., Su, Y., Schilling, J.G., 2013. The mean composition of ocean ridge basalts. Geochemistry, Geophysics, Geosystems 14, 489–518. doi:10.1029/2012GC004334.

Gamaleldien, H., Wu, L.G., Olierook, H.K., Kirkland, C.L., Kirscher, U., Li, Z.X., Johnson, T.E., Makin, S., Li, Q.L., Jiang, Q., Wilde, S.A., Li, X.H., 2024. Onset of the Earth's hydrological cycle four billion years ago or earlier. Nature Geoscience 2024 17:6 17, 560–565. doi:10.1038/s41561-024-01450-0.

Gast, P.W., 1968. Trace element fractionation and the origin of tholeiitic and alkaline magma types. Geochimica et Cosmochimica Acta 32, 1057–1086. doi:10.1016/0016-7037(68)90108-7.

Geological Survey of Western Australia, 2021. WACHEM database. URL: https://www.wa.gov.au/service/natural-resources/mineral-resources/access-geochemistry accessed 2019–2021.

Griffin, W., O'Reilly, S., Ryan, C., 1999. The composition and origin of subcontinental lithospheric mantle, in: Mantle Petrology: Field Observations and High Pressure Experimentation: A Tribute to Francis R. (Joe) Boyd. Geochemical Society Special Publication, Geochemical Society, Houston, pp. 13–45. URL: https://www.geochemsoc.org/files/5614/1270/3112/SP-6_013-046_Griffin.pdf.

Hastie, A.R., Fitton, J.G., Bromiley, G.D., Butler, I.B., Odling, N.W., 2016. The origin of Earth's first continents and the onset of plate tectonics. Geology 44, 855–858. doi:10.1130/G38226.1.

Hawkesworth, C., Cawood, P., Kemp, T., Storey, C., Dhuime, B., 2009. A matter of preservation. Science 323, 49–50. doi:10.1126/science.1168549.

Herzberg, C., Condie, K., Korenaga, J., 2010. Thermal history of the Earth and its petrological expression. Earth and Planetary Science Letters 292, 79–88. doi:10.1016/j.epsl.2010.01.022.

Herzberg, C., Rudnick, R., 2012. Formation of cratonic lithosphere: An integrated thermal and petrological model. Lithos 149, 4–15. doi:10.1016/J.LITHOS.2012.01.010.

Hofmann, A.W., Feigenson, M.D., 1983. Case studies on the origin of basalt. Contributions to Mineralogy and Petrology 84, 382–389. doi:10.1007/BF01160289.

Hofmann, A.W., Jochum, K.P., Seufert, M., White, W.M., 1986. Nb and Pb in oceanic basalts: new constraints on mantle evolution. Earth and Planetary Science Letters 79, 33–45. doi:10.1016/0012-821X(86)90038-5.

Hoggard, M.J., Czarnota, K., Richards, F.D., Huston, D.L., Jaques, A.L., Ghelichkhan, S., 2020. Global distribution of sediment-hosted metals controlled by craton edge stability. Nature Geoscience 13, 504–510. doi:10.1038/s41561-020-0593-2.

Hopkins, M.D., Harrison, T.M., Manning, C.E., 2010. Constraints on Hadean geodynamics from mineral inclusions in ¿ 4 Ga zircons. Earth and Planetary Science Letters 298, 367–376. doi:10.1016/J.EPSL.2010.08.010.

Jarvis, G.T., Campbell, I.H., 1983. Archean komatiites and geotherms: Solution to an apparent contradiction. Geophysical Research Letters 10, 1133–1136. doi:10.1029/GL010i012p01133.

Jennings, E.S., Holland, T.J., 2015. A simple thermodynamic model for melting of peridotite in the system NCFMASOCr. Journal of Petrology 56, 869–892. doi:10.1093/petrology/egv020.

Jochum, K.P., Seufert, H.M., Spettel, B., Palme, H., 1986. The solar-system abundances of Nb, Ta, and Y, and the relative abundances of refractory lithophile elements in differentiated planetary bodies. Geochimica et Cosmochimica Acta 50, 1173–1183. doi:10.1016/0016-7037(86)90400-X.

Kankanamge, D.G., Moore, W.B., 2016. Heat transport in the Hadean mantle: From heat pipes to plates. Geophysical Research Letters 43, 3208–3214. doi:10.1002/2015GL067411.

Kasting, J.F., Catling, D., 2003. Evolution of a habitable planet. Annual Review of Astronomy and Astrophysics 41, 429–463. doi:10.1146/annurev.astro.41.071601.170049.

Katz, R.F., Spiegelman, M., Langmuir, C.H., 2003. A new parameterization of hydrous mantle melting. Geochemistry, Geophysics, Geosystems 4, 1–19. doi:10.1029/2002GC000433.

Kay, R.W., Gast, P.W., 1973. The rare earth content and origin of alkali-rich basalts. The Journal of Geology 81, 653–682.

Keller, B., Schoene, B., 2018. Plate tectonics and continental basaltic geochemistry throughout earth history. Earth and Planetary Science Letters 481, 290–304. doi:10.1016/j.epsl.2017.10.031.

Kennett, B.L.N., Chopping, R., Blewett, R.S., 2018. The Australian Continent: A Geophysical Synthesis. ANU Press. URL: `http://www.jstor.org/stable/j.ctv69tg79`.

Klöcking, M., Czarnota, K., Champion, D., Jaques, A., Davies, D.R., 2020. Spatiotemporal evolution of Australian lithosphere-asthenosphere boundary from mafic volcanism, in: Czarnota, K., Roach, I., Abbott, S., Haynes, M., Kositcin, N., Ray, A., Slatter, E. (Eds.), Exploring for the Future: Extended Abstracts. Geoscience Australia, Canberra, pp. 1–4. doi:10.11636/135075.

Klöcking, M., White, N.J., Maclennan, J., McKenzie, D., Fitton, J.G., 2018. Quantitative relationships between basalt geochemistry, shear wave velocity, and asthenospheric temperature beneath western North America. Geochemistry, Geophysics, Geosystems 19, 3376–3404. doi:10.1029/2018GC007559.

[software] Klöcking, M., 2025. Software for 'Archaean basalts record evidence of lithospheric extension prior to cratonisation'. URL: `https://github.com/mk618/Yilgarn-mafics`, doi:TBC (Zenodo).

[dataset] Klöcking, M., Champion, D.C., Smithies, R.H., Lowrey, J.R., Norman, M.D., 2025. Compilation of mafic igneous rock compositions from Australia (Archaean to Quaternary ages). GFZ Data Services. doi:10.5880/digis.e.2025.001.

Korenaga, J., 2013. Initiation and evolution of plate tectonics on earth: Theories and observations. Annual Review of Earth and Planetary Sciences 41, 117–151. doi:10.1146/annurev-earth-050212-124208.

Korhonen, F.J., Kelsey, D.E., Ivanic, T.J., Blereau, E.R., Smithies, R., De Paoli, M.C., Fielding, I.O., 2025. Radiogenic heat production provides a thermal threshold for Archean cratonization process. Geology 53, 222–226. doi:10.1130/G52755.1.

Kositcin, N., Brown, S.J., Barley, M.E., Krapež, B., Cassidy, K.F., Champion, D.C., 2008. SHRIMP U-Pb zircon age constraints on the Late Archaean tectonostratigraphic architecture of the Eastern Goldfields Superterrane, Yilgarn Craton, Western Australia. Precambrian Research 161, 5–33. doi:10.1016/j.precamres.2007.06.018.

Krapez, B., Brown, S., Hand, J., Barley, M., Cas, R., 2000. Age constraints on recycled crustal and supracrustal sources of Archaean metasedimentary sequences, Eastern Goldfields Province, Western Australia: evidence from SHRIMP zircon dating. Tectonophysics 322, 89–133. doi:10.1016/S0040-1951(00)00059-7.

Langmuir, C.H., Klein, E.M., Plank, T., 1992. Petrological Systematics of Mid-Ocean Ridge Basalts: Constraints on Melt Generation Beneath Ocean Ridges. Mantle Flow and Melt Generation at Mid-Ocean Ridges 71, 183–280. doi:10.1029/GM071p0183.

Lee, C.T.A., Caves, J., Jiang, H., Cao, W., Lenardic, A., McKenzie, N.R., Shorttle, O., zhu Yin, Q., Dyer, B., 2018. Deep mantle roots and continental emergence: implications for whole-earth elemental cycling, long-term climate, and the Cambrian explosion. International Geology Review 60, 431–448. doi:10.1080/00206814.2017.1340853.

Lee, C.T.A., Chin, E.J., 2014. Calculating melting temperatures and pressures of peridotite protoliths: Implications for the origin of cratonic mantle. Earth and Planetary Science Letters 403, 273–286. doi:10.1016/J.EPSL.2014.06.048.

Lee, C.T.A., Luffi, P., Plank, T., Dalton, H., Leeman, W.P., 2009. Constraints on the depths and temperatures of basaltic magma generation on Earth and other terrestrial planets using new thermobarometers for mafic magmas. Earth and Planetary Science Letters 279, 20–33. doi:10.1016/j.epsl.2008.12.020.

Lesher, C.M., Arndt, N.T., 1995. REE and Nd isotope geochemistry, petrogenesis and volcanic evolution of contaminated komatiites at Kambalda, Western Australia. Lithos 34, 127–157. doi:10.1016/0024-4937(95)90017-9.

Matthews, S., Wong, K., Gleeson, M., 2022. pyMelt: An extensible Python engine for mantle melting calculations. Volcanica 5, 469–475. doi:10.30909/vol.05.02.469475.

McDonough, W.F., Sun, S.s., 1995. The composition of the Earth. Chemical Geology 120, 223–253. doi:10.1016/0009-2541(94)00140-4.

McKenzie, D., Bickle, M.J., 1988. The volume and composition of melt generated by extension of the lithosphere. Journal of Petrology 29, 625–679. doi:10.1093/petrology/29.3.625.

McKenzie, D., O'Nions, R.K., 1991. Partial melt distributions from inversion of rare earth element concentrations. Journal of Petrology 32, 1021–1091. doi:10.1093/petrology/32.5.1021.

McKenzie, D., O'Nions, R.K., 1995. The Source Regions of Ocean Island Basalts. Journal of Petrology 36, 133–159. doi:10.1093/petrology/36.1.133.

Michael, P., 1995. Regionally distinctive sources of depleted MORB: Evidence from trace elements and H_2O. Earth and Planetary Science Letters 131, 301–320. doi:10.1016/0012-821X(95)00023-6.

Minster, J.F., Allègre, C.J., 1978. Systematic use of trace elements in igneous processes. Contributions to Mineralogy and Petrology 68, 37–52. doi:10.1007/BF00375445.

Mole, D., Kirkland, C., Fiorentini, M., Barnes, S., Cassidy, K., Isaac, C., Belousova, E., Hartnady, M., Thebaud, N., 2019. Time-space evolution of an Archean craton: A Hf-isotope window into continent formation. Earth-Science Reviews 196, 102831. doi:10.1016/j.earscirev.2019.04.003.

Moore, W.B., Webb, A.A.G., 2013. Heat-pipe earth. Nature 501, 501–505. doi:10.1038/nature12473.

Moyen, J.F., Laurent, O., 2018. Archaean tectonic systems: A view from igneous rocks. Lithos 302-303, 99–125. doi:10.1016/j.lithos.2017.11.038.

Moyen, J.F., Martin, H., 2012. Forty years of TTG research. Lithos 148, 312–336. doi:10.1016/j.lithos.2012.06.010.

Nelson, D.R., 1997. Evolution of the Archaean granite-greenstone terranes of the Eastern Goldfields, Western Australia: SHRIMP U-Pb zircon constraints. Precambrian Research 83, 57–81. doi:10.1016/S0301-9268(97)00005-3.

Nesbitt, R.W., Sun, S.S., 1976. Geochemistry of Archaean spinifex-textured peridotites and magnesian and low-magnesian tholeiites. Earth and Planetary Science Letters 31, 433–453. doi:10.1016/0012-821X(76)90125-4.

Nisbet, E.G., Cheadle, M.J., Arndt, N.T., Bickle, M.J., 1993. Constraining the Potential Temperature of the Archean Mantle - a Review of the Evidence from Komatiites. Lithos 30, 291–307. doi:10.1016/0024-4937(93)90042-B.

Occhipinti, S., Hocking, R., Lindsay, M., Aitken, A., Copp, I., Jones, J., Sheppard, S., Pirajno, F., Metelka, V., 2017. Paleoproterozoic basin development on the northern Yilgarn Craton, Western Australia. Precambrian Research 300, 121–140. doi:10.1016/j.precamres.2017.08.003.

Oliveira, B., Afonso, J.C., Tilhac, R., 2020. A disequilibrium reactive transport model for mantle magmatism. Journal of Petrology doi:10.1093/petrology/egaa067.

O'Neill, C., Debaille, V., 2014. The evolution of Hadean–Eoarchaean geodynamics. Earth and Planetary Science Letters 406, 49–58. doi:10.1016/j.epsl.2014.08.034.

Oversby, V., 1975. Lead isotopic systematics and ages of Archaean acid intrusives in the Kalgoorlie-Norseman area, Western Australia. Geochimica et Cosmochimica Acta 39, 1107–1125. doi:10.1016/0016-7037(75)90053-8.

Pawley, M.J., Wingate, M.T.D., Kirkland, C.L., Wyche, S., Hall, C.E., Romano, S.S., Doublier, M.P., 2012. Adding pieces to the puzzle: episodic crustal growth and a new terrane in the northeast Yilgarn Craton, Western Australia. Australian Journal of Earth Sciences 59, 603–623. doi:10.1080/08120099.2012.696555.

Plank, T., Forsyth, D.W., 2016. Thermal structure and melting conditions in the mantle beneath the Basin and Range province from seismology and petrology. Geochemistry, Geophysics, Geosystems 17, 1312–1338. doi:10.1002/2015GC006205.

Redman, B., Keays, R.R., 1985. Archaean basic volcanism in the Eastern Goldfields Province, Yilgarn Block, Western Australia. Precambrian Research 30, 113–152. doi:10.1016/0301-9268(85)90048-8.

Richter, F.M., 1988. A Major Change in the Thermal State of the Earth at the Archean-Proterozoic Boundary: Consequences for the Nature and Preservation of Continental Lithosphere. Journal of Petrology Special Volume, 39–52. doi:10.1093/petrology/Special_Volume.1.39.

Said, N., Kerrich, R., Groves, D., 2010. Geochemical systematics of basalts of the Lower Basalt Unit, 2.7 Ga Kambalda Sequence, Yilgarn craton, Australia: Plume impingement at a rifted craton margin. Lithos 115, 82–100. doi:10.1016/J.LITHOS.2009.11.008.

Shorttle, O., Maclennan, J., Lambart, S., 2014. Quantifying lithological variability in the mantle. Earth and Planetary Science Letters 395, 24–40. doi:10.1016/j.epsl.2014.03.040.

Smithies, R., Gessner, K., Lu, Y., Kirkland, C., Ivanic, T., Lowrey, J., Champion, D., Sapkota, J., Masurel, Q., Thébaud, N., de Gromard, R.Q., 2024. Geochemical mapping of lithospheric architecture disproves Archean terrane accretion in the Yilgarn craton. Geology 52, 141–146. doi:10.1130/G51707.1.

Smithies, R.H., Lowrey, J.R., Sapkota, J., Paoli, M.C.D., Hayman, P., Barnes, S.J., Champion, D.C., Masurel, Q., Thébaud, N., Grech, L.L., Drummond, M., Maas, R., 2022. Geochemical characterization of the magmatic stratigraphy of the Kalgoorlie and Black Flag Groups, Ora Banda to Kambalda region. Report 226, Geological Survey of Western Australia.

Stern, R.J., 2005. Evidence from ophiolites, blueschists, and ultrahigh-pressure metamorphic terranes that the modern episode of subduction tectonics began in Neoproterozoic time. Geology 33, 557–560. doi:10.1130/G21365.1.

Swager, C.P., 1997. Tectono-stratigraphy of late Archaean greenstone terranes in the southern Eastern Goldfields, Western Australia. Precambrian Research 83, 11–42. doi:10.1016/S0301-9268(97)00003-X.

Sylvester, P.J., Campbell, I.H., Bowyer, D.A., 1997. Niobium/uranium evidence for early formation of the continental crust. Science 275, 521–523. doi:10.1126/science.275.5299.521.

Tesauro, M., Kaban, M.K., Aitken, A.R.A., 2020. Thermal and compositional anomalies of the Australian upper mantle from seismic and gravity data. Geochemistry, Geophysics, Geosystems 21. doi:10.1029/2020GC009305.

Thorne, J., Highet, L., Cooper, M., Claoue-Long, J., Hoatson, D., Jaireth, S., Huston, D., Gallagher, R.G., 2014. Australian Mafic-Ultramafic Magmatic Events GIS Dataset, 1:5 000 000 scale [Digital Dataset]. Geoscience Australia. doi:10.11636/Record.2014.039.

Walter, M.J., 1998. Melting of garnet peridotite and the origin of komatiite and depleted lithosphere. Journal of Petrology 39, 29–60. doi:10.1093/petroj/39.1.29.

Westrenen, W., Wood, B.J., Blundy, J.D., 2001. A predictive thermodynamic model of garnet–melt trace element partitioning. Contributions to Mineralogy and Petrology 142, 219–234. doi:10.1007/s004100100285.

White, R.S., McKenzie, D., O'Nions, R.K., 1992. Oceanic crustal thickness from seismic measurements and rare earth element inversions. Journal of Geophysical Research 97, 19683. doi:10.1029/92JB01749.

Wood, B.J., Blundy, J.D., 1997. A predictive model for rare earth element partitioning between clinopyroxene and anhydrous silicate melt. Contributions to Mineralogy and Petrology 129, 166–181. doi:10.1007/s004100050330.